Fusion Engineering and Design 230 (2026) 115844

Contents lists available at ScienceDirect

Fusion Engineering and Design

journal homepage: www.elsevier.com/locate/fusengdes

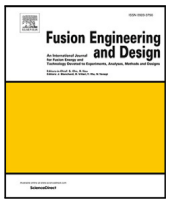

Investigation of wall boiling models for fusion-relevant high heat and mass flux flow conditions

Ahmet Kılavuz [a,b,*], Boštjan Koncar [c], Jeong-Ha You [b], Rudolf Neu [a,b]

[a] Technical University of Munich, Garching, Germany
[b] Max Planck Institute for Plasma Physics, Garching, Germany
[c] Reactor Engineering Division, Jozef Stefan Institute, Ljubljana, Slovenia

ARTICLE INFO

Keywords:
Heat transfer
High heat flux
Subcooled flow boiling
Wall boiling models
Fusion

ABSTRACT

Subcooled flow boiling in plasma-facing component cooling structures can occur under extreme conditions with heat fluxes reaching 50 MW m^{-2} and mass fluxes up to 20,000 kg m^{-2} s^{-1}. To date, comprehensive large-dataset comparisons assessing the suitability of wall boiling frameworks for fusion-relevant conditions remain limited. This study investigates wall boiling models under fusion-relevant high heat- and mass-flux conditions. The Rensselaer Polytechnic Institute (RPI) and Massachusetts Institute of Technology Boiling (MITB) models are analyzed together with various boiling-parameter correlations using a database of 387 experimental measurements obtained from fusion-relevant campaigns. The analysis shows that the RPI framework exhibits intrinsic limitations at elevated mass fluxes ($G > 4000$ kg m^{-2} s^{-1}), producing non-physical negative boiling-curve gradients in the partially developed nucleate boiling regime. Systematic variation of bubble-parameter models demonstrates that this behavior cannot be resolved solely by adjusting boiling-parameter correlations, indicating a framework-level limitation. It is found that the observed behavior arises from excessive suppression of the convective heat-flux contribution in the bubble-coverage formulation. The MITB model mitigates this limitation through a sliding-conduction mechanism and bubble-coverage representation, yielding physically consistent predictions across all investigated conditions and reducing the mean absolute error in wall-superheat prediction by approximately 85% compared with generic RPI implementations under high mass- and heat-flux conditions. These findings provide guidance on wall boiling model selection for two-phase analyses of high-heat-flux cooling applications, such as divertor targets.

1. Introduction

1.1. Subcooled flow boiling

Subcooled flow boiling occurs when vapor bubbles form on a heated wall while the flowing bulk liquid remains below the saturation temperature. In this regime, nucleate boiling can remove large heat fluxes at low wall superheats, and the resulting heat transfer coefficients (HTC) can exceed single-phase forced convection. With a higher heat flux, nucleation progresses and spreads until the majority of potential nucleation sites on the wall are active. This leads to an increasing trend of vapor generation towards fully developed nucleate boiling (FDNB). At the critical heat flux (CHF), departure from nucleate boiling (DNB) occurs, branching off along the FDNB trend as local vapor films cover parts of the wall. At DNB, the heat transfer coefficients decline dramatically, and small increases in wall heat flux produce a large rise in wall temperature.

Due to its capability of removing high heat fluxes at low superheats and its high thermo-hydraulic performance factor, nucleate boiling is widely used across industrial systems, nuclear reactors, and power electronics. However, operating below CHF is essential to avoid component failure. Therefore, utilizing enhanced heat transfer of boiling is a complex task that requires extensive knowledge and understanding of the phenomena. However, since the thermo-hydraulic behavior of nucleate boiling strongly depends on parameters regarding flow, wall surface, and geometry, developing a quantitative model remains challenging. Datasets and correlations cover standard industrial ranges but become sparse under extreme flow conditions such as high heat and mass fluxes, constraining model development and verification. These uncertainties drive conservative design margins, reducing allowable heat loads and system efficiency. One example case is plasma-facing components (PFCs) in fusion devices.

* Corresponding author at: Max Planck Institute for Plasma Physics, Garching, Germany.
E-mail address: ahmet.kilavuz@ipp.mpg.de (A. Kılavuz).

https://doi.org/10.1016/j.fusengdes.2026.115844
Received 23 February 2026; Received in revised form 14 April 2026; Accepted 28 May 2026
Available online 3 June 2026

Nomenclature

Latin symbols

A	Area [m^2]	L	Heated length [m]
D	Diameter [m]	D_h	Hydraulic diameter [m]
D_d	Bubble departure diameter [m]	f_d	Bubble departure frequency [s^{-1}]
G	Mass flux [$kg\,m^{-2}\,s^{-1}$]	N_a	Nucleation-site density [m^{-2}]
h	Heat-transfer coefficient [$W\,m^{-2}K^{-1}$]	h_{fg}	Latent heat [$J\,kg^{-1}$]
q''	Heat flux [$W\,m^{-2}$]	$\dot{q}_C$	Convective heat flux [$W\,m^{-2}$]
$\dot{q}_E$	Evaporation heat flux [$W\,m^{-2}$]	$\dot{q}_{SC}$	Sliding-conduction heat flux [$W\,m^{-2}$]
$\dot{q}_{SQ}$	Solid-quenching heat flux [$W\,m^{-2}$]	$\dot{q}_Q$	Quenching heat flux [$W\,m^{-2}$]
R_c	Critical cavity radius [m]	u	Velocity [$m\,s^{-1}$]
K_{bubble}	Bubble influence factor [–]	Ca	Capillary number [–]
Ja	Jakob number [–]	Nu	Nusselt number [–]
Pr	Prandtl number [–]	ΔT_{sub}	Subcooling [K]
$\Delta T_{\text{sat,w}}$	Wall Superheat [K]		

Greek symbols

α	Thermal diffusivity [$m^2\,s^{-1}$]	σ	Surface tension [$N\,m^{-1}$]
λ	Thermal conductivity [$W\,m^{-1}K^{-1}$]	μ	Dynamic viscosity [Pa s]
ρ	Density [$kg\,m^{-3}$]	θ	Contact angle [deg, rad]

Subscripts

bulk	Bulk fluid	liquid	Liquid phase
vapor	Vapor phase	wall	Wall
sat	Saturation state	sliding	Sliding region
lift-off	Bubble lift-off	microlayer	Microlayer

1.2. Subcooled flow boiling in fusion

In fusion applications, PFCs are exposed to extreme flow and thermal loads. Among these components, divertor targets operate under some of the most severe conditions, designed to handle intense heat and particle fluxes from the plasma. During quasi-stationary EU DEMO operation, divertor heat-flux loads are around 10 $MW\,m^{-2}$. Transient strike-point reattachment can raise local heat fluxes to approximately 20 $MW\,m^{-2}$ for durations of about 10 s, while shorter events (< 10 s) may lead to peak heat loads exceeding 50 $MW\,m^{-2}$, even with strike-point sweeping [1]. To maintain thermo-structural integrity under such conditions, an efficient cooling system with low pumping power is desirable. Water is the baseline coolant in the EU DEMO divertor design [1] and is also considered for other components, such as breeding blankets [2]. Due to design constraints, such as embrittlement under neutron irradiation and corrosion, complete avoidance of boiling in PFCs is difficult to achieve [3]. Consequently, nucleate boiling must be accounted for in the thermal design of these systems, and models should accurately predict the associated heat fluxes. Improved predictive capability for boiling is essential for a more reliable assessment of safety margins and power losses. Therefore, evaluating existing nucleate boiling models under fusion-relevant flow conditions is necessary for their effective use as design tools.

1.3. Nucleate boiling models

Two approaches dominate nucleate boiling heat flux prediction below CHF. Firstly, empirical total-heat-flux correlations. Second, a semi-mechanistic heat-flux partitioning approach, also known as wall boiling models. Empirical correlations have been developed for fusion-relevant flow conditions, such as those from JAERI (Araki) [4] and CEA (Thom–CEA) [5] for ITER divertors. Additionally, more recent models developed by Yan for uniform heating [6] and Zhu for one-sided heating in twisted-tape inserts [7] are relatively accurate within their specific geometries and development ranges. However, developing new empirical correlations requires extensive experimental campaigns for each geometry and operating condition, making them costly and time-consuming design tools. In contrast, the heat-flux partitioning approach provides wider applicability across geometries and provides a clearer link to underlying mechanisms. These models can be integrated with computational fluid dynamics (CFD) to predict spatially and temporally resolved fields like wall temperature, wall heat flux, vapor fraction, and pressure drop in flow-boiling systems [8].

1.3.1. Heat-flux partitioning approach

Kurul and Podowski formalized the mechanisms of nucleate boiling with the RPI wall boiling model. The model partitions the wall heat flux into convection, quenching, and evaporation using temporally and spatially averaged relations. Each partition term has its own set of equations to represent the underlying process [9]. Later, Gilman et al. developed the MIT Boiling (MITB) model by significantly modifying the RPI framework to establish a more physics-based and generalizable formulation and validated it for heat fluxes up to 5 $MW\,m^{-2}$ [10, 11]. However, both frameworks require additional bubble parameters, such as active nucleation site density, bubble departure frequency, and bubble departure diameter, to close the equations for the heat-partition terms. These parameters are highly dependent on flow parameters, such as pressure, subcooling, and wall superheat. Due to the sensitivity of these bubble parameters to flow conditions, evaluating PWR-based correlations under fusion-relevant conditions, is essential. Studies applying wall boiling models to fusion-relevant flow conditions are limited. Liu et al. [12] evaluated the RPI wall boiling model in CFD under divertor-target without swirl-tapes, using a single condition set at $8,000\ kg\,m^{-2}\,s^{-1}$ low subcooling (57 K). Yu [13] performed a similar analysis for different channel structures with wall boiling models tested against Araki's correlation. They compared six flow condition sets with mass fluxes below $10,000\ kg\,m^{-2}\,s^{-1}$ and moderate subcooling (70–90 K). However, rigorous evaluation of such models requires large, diverse datasets across many flow conditions to avoid spurious accuracy on isolated cases. Recently, Končar et al. [14] reported non-physical predictions from the RPI wall boiling model, which uses conventional bubble-parameter correlations, at higher mass fluxes under multiple flow conditions. EU DEMO divertor-relevant flow conditions span subcooling of 20–160 K and velocities of 5–17 $m\,s^{-1}$. A systematic evaluation across these fusion-relevant conditions, with a large number of data points, has not yet been reported to the best of the authors' knowledge.

1.4. Past experimental campaigns

Fusion-relevant experimental data for evaluating and validating wall boiling models are scarce. Ideally, robust validation requires comparison of model predictions of volume fractions, bubble parameters, and wall temperatures with detailed measurements. However, under fusion-relevant flow conditions, no such measurements of volume fractions or bubble parameters exist to the author's knowledge. The Jožef Stefan Institute (JSI) has initiated efforts to develop scaled-down facilities equipped with advanced visualization tools to capture the mentioned quantities under fusion-relevant conditions, but substantial data are not yet available [15]. Therefore, current validations rely on wall-temperature measurements. These measurements are limited to ITER-relevant conditions obtained with systematic thermo-hydraulic campaigns. Excluding the more extensively studied critical heat flux datasets, the number of available nucleate boiling heat transfer measurements remains small.

At JAERI and CEA, experiments were conducted under fusion-relevant flow conditions to develop a fully developed nucleate boiling model for ITER divertors [4,5,16]. Later, the Moscow Power Engineering Institute conducted an extensive campaign to develop a database on both nucleate boiling heat transfer and the critical heat flux regime in one-sided twisted-tape cooling under fusion-relevant conditions [17,18]. More recently, Yan et al. investigated subcooled flow boiling in tubes with and without twisted tapes at high heat fluxes [6,19]. Later, the same group examined flow boiling under one-sided heating in swirl-tape and smooth-pipe configurations and proposed empirical correlations [7,20]. Lim et al. also conducted experiments with twisted tapes and one-sided heating, though at lower heat and mass fluxes [21].

1.5. Scope and purpose

Future divertor targets, such as those foreseen for the European DEMO, will operate under extreme flow conditions: pressures of 0.5–5 MPa, subcoolings of 10–200 K, mass fluxes of 5000–20, 000 $\mathrm{kg\,m^{-2}\,s^{-1}}$, and heat fluxes exceeding 50 $\mathrm{MW\,m^{-2}}$. The mass and heat fluxes exceed the range of existing pressurized-water-reactor (PWR) databases, where wall boiling models have traditionally been developed and calibrated. Therefore, the applicability of such models to fusion-relevant flow conditions remains uncertain.

To address this, the present study investigates the performance of wall boiling models under high mass and heat fluxes relevant to EU DEMO, focusing on the RPI and MITB heat-partitioning frameworks. Particular attention will be given to the sensitivity of models to key bubble-parameter correlations, including departure diameter, departure frequency, and nucleation-site density.

Comprehensive experimental datasets, including data from both uniform and non-uniform heating, as well as smooth and swirl-tape inserted cooling tubes, are used to evaluate model performance and physical consistency across a broad flow and geometry parameter space. The objective is to identify a wall boiling model framework suitable for reliable integration into divertor design tools and future CFD frameworks. The study also aims to define the limitations and required improvements of current wall boiling models under fusion-relevant high heat and mass fluxes.

2. Model

2.1. RPI wall boiling model

The RPI model captures the different heat transfer modes during the bubble ebullition cycle by partitioning the wall heat flux into distinct mechanisms:

$$\dot{q}_W = \dot{q}_C + \dot{q}_Q + \dot{q}_E \tag{1}$$

Here, the terms on the right-hand side represent the heat flux due to liquid convection ($\dot{q}_C$), quenching ($\dot{q}_Q$), and evaporation ($\dot{q}_E$).

Convection heat flux accounts for the single-phase liquid heat transfer to the portion of the wall not influenced by bubbles. It is calculated as

$$\dot{q}_C = (1 - A_b)\, h_c\, (T_w - T_l) \tag{2}$$

where h_c is the single-phase convection heat-transfer coefficient. A_b is the bubble-influenced area fraction, given by [22]

$$A_b = \min\left(1,\, \pi \left(K_i \frac{D_d}{2}\right)^2 N_a\right). \tag{3}$$

Here, N_a is the active nucleation site density, D_d is the bubble departure diameter, and K_i is the influence factor (taken as $K_i = 2$ following Kurul [9]). Experiments by Han and Griffith [23] and Cieśliński [24] showed that the disturbance field created by a bubble extends to roughly twice its size.

The quenching heat flux arises from cooler liquid rushing toward the wall after bubble departure and is expressed as [9]

$$\dot{q}_Q = h_Q A_b (T_w - T_l), \tag{4}$$

where the quenching heat-transfer coefficient is modeled by Mikic and Rohsenow [25] as

$$h_Q = \frac{2}{\sqrt{\pi}}\, f\, \sqrt{t_W\, k_l\, \rho_l\, C_{p,l}}. \tag{5}$$

Here, f is the bubble departure frequency and t_W the waiting time between bubble departure and nucleation.

Finally, the evaporation heat flux accounts for phase change due to vapor generation:

$$\dot{q}_E = \frac{\pi D_d^3}{6}\, \rho_g\, f\, N_a\, h_{lg}, \tag{6}$$

where ρ_g is the vapor density and h_{lg} the latent heat of vaporization.

In summary, closure relations are required for the bubble parameters N_a, D_d, and f, which will be introduced and investigated in this study.

2.2. MITB wall boiling model

The Massachusetts Institute of Technology Boiling (MITB) model replaces the RPI wall boiling model by introducing additional mechanisms such as bubble sliding, microlayer evaporation, and transient solid quenching [10]. The total wall heat flux is expressed as

$$\dot{q}_W = \dot{q}_C + \dot{q}_{SC} + \dot{q}_E + \dot{q}_{SQ}, \tag{7}$$

where $\dot{q}_C$ denotes the convective heat flux, $\dot{q}_{SC}$ the sliding-conduction term, $\dot{q}_E$ the evaporation term, and $\dot{q}_{SQ}$ the solid-quenching contribution.

The convective heat flux represents single-phase liquid convection over the wall area not covered by active bubbles:

$$\dot{q}_C = (1 - S_{sl})\, h_c\, (T_w - T_l), \tag{8}$$

where h_c is the single-phase convective heat-transfer coefficient and S_{sl} the time-averaged sliding-coverage fraction.

The fraction of the surface influenced by bubble sliding is obtained from geometric and temporal considerations. The instantaneous sliding-area fraction is approximated as

$$A_{sl} = \min\left(1,\, \frac{1}{\sqrt{N_a}} \left(\frac{D_{lo} + D_d}{2}\right)\right). \tag{9}$$

where D_d is the bubble-departure diameter, D_{lo} the bubble lift-off diameter, and N_a the active nucleation-site density. The time-averaged sliding coverage is then estimated as

$$S_{sl} = \min\left(A_{sl}\, N_a\, t^*\, f,\, 1\right), \tag{10}$$

with f the bubble-departure frequency and t^* the characteristic thermal-diffusion time,

$$t^* = \frac{(\lambda/h_c)^2}{\pi\,\alpha_l}, \qquad \alpha_l = \frac{\nu}{\mathrm{Pr}}. \tag{11}$$

As bubbles slide along the wall, transient conduction occurs between the liquid and the wall within the covered region:

$$\dot{q}_{SC} = 2\,h_c\,S_{sl}\,(T_w - T_l). \tag{12}$$

This mechanism enhances near-wall heat transfer through repeated contact and rewetting cycles under sliding bubbles.

The evaporation component consists of vapor generation during bubble inception and microlayer evaporation beneath the bubble:

$$\dot{q}_E = \dot{q}_{\mathrm{inception}} + \dot{q}_{\mathrm{microlayer}}, \tag{13}$$

$$\dot{q}_{\mathrm{inception}} = \frac{4}{3}\pi\left(\frac{D_{\mathrm{inception}}}{2}\right)^3 \rho_g\,h_{lg}\,f\,N_a, \tag{14}$$

$$\dot{q}_{\mathrm{microlayer}} = V_{\mathrm{ml}}\,\rho_l\,h_{lg}\,f\,N_a. \tag{15}$$

where $D_{\mathrm{inception}}$ is the inception diameter and V_{ml} the microlayer volume. The microlayer thickness δ_{ml} and dryout ratio are correlated with the capillary number $Ca = \mu_l\,U_{bg}/\sigma$, where U_{bg} is the bubble-growth velocity and σ the surface tension.

In addition to liquid-based effects, the MITB model introduces a solid-quenching term to represent transient conduction in the wall material during bubble rewetting:

$$\dot{q}_{SQ} = \frac{2}{3}\pi\,\rho_s\,C_{p,s}\left(\frac{D_{\mathrm{dry}}}{2}\right)^2 f\,N_a\,\Delta T_h, \tag{16}$$

where ρ_s and $C_{p,s}$ are the density and specific heat of the wall material, respectively, D_{dry} is the dry-region diameter, and ΔT_h is the characteristic temperature difference driving transient solid conduction, which was proposed to be approximately 2 K [10].

2.3. Solver details

A solver was developed to compute wall superheats using wall boiling models with inputs from experimental thermal measurements (e.g., heat flux, temperatures), flow parameters (e.g., mass flux, pressure), and geometric data (e.g., tube diameter, heated length, twist ratio, swirl tape thickness). Thermo-physical properties of water are calculated through the `XSteam` library using the measured pressure p, wall temperature T_w, and inlet liquid temperature T_l.

The solver includes both the RPI and MITB heat-partitioning models together with their associated bubble-parameter submodels. For the single-phase heat-transfer coefficient required by the wall boiling models, a swirl-corrected Gnielinski correlation can be used. The correction employs a swirl-enhanced Reynolds number defined as $Re_{\mathrm{sw}} = \kappa Re$, with $\kappa = 1$ for a plain tube. For a swirl-tape channel, κ is given by

$$\kappa = \sqrt{1 + \frac{\pi^2}{4\,y^2}}. \tag{17}$$

The heat-transfer coefficient is evaluated from [26]

$$h = \frac{\lambda}{D_h}\,\frac{\frac{f}{8}\,(Re_{\mathrm{sw}} - 1000)\,Pr_{\mathrm{b}}}{1 + 12.7\sqrt{\frac{f}{8}}\left(Pr_{\mathrm{b}}^{2/3} - 1\right)}\left(\frac{\mu_{\mathrm{b}}}{\mu_{\mathrm{w}}}\right)^{0.11}\left[1 + \left(\frac{D_h}{L}\right)^{2/3}\right], \tag{18}$$

where the friction factor is

$$f = \left(1.82\ln(Re_{\mathrm{sw}}) - 1.64\right)^{-2}.$$

Another method to obtain the single-phase heat-transfer coefficient h is to extract it directly from the available experimental data at the negative wall superheat closest to zero. This approach minimizes dependence on single-phase correlations and allows a more direct assessment of the wall boiling models; for this reason, the present study uses experimentally derived single-phase convection coefficients. On the other hand, the effect of calculating heat transfer coefficients by Gnielinski correlation on the models is also examined in Section 5. The wall superheat is computed by solving the heat-flux residual equation, in which the difference between the measured and model-predicted total heat fluxes approaches zero:

$$F(\Delta T) = \dot{q}_{\mathrm{model}}(\Delta T) - \dot{q}_{\mathrm{exp}} \to 0.$$

A bounded root-finding algorithm is used to ensure convergence. Using the thermo-hydraulic measurement database as input, the model is provided with measured quantities (e.g., local wall temperature, bulk inlet temperature, mass flux, pressure, and average flow velocity). The solver provides wall boiling model predictions that form the basis for the subsequent investigations. The uncertainty in the calculated wall superheat is obtained using the upper–lower bound method, in which the residual equation is solved at the upper and lower bounds of the measured heat flux:

$$\Delta T_w \pm \delta(\Delta T_w) = F^{-1}\left(\dot{q}_{\mathrm{exp}} \pm \delta\dot{q}_{\mathrm{exp}}\right), \tag{19}$$

To validate the solver, in Fig. 1, the MITB model predictions are compared against the subcooled boiling experiments of Kennel [27], specifically the works of Carl and Picornell. High-mass-flux run was excluded because the test was reported to remain close to ONB, providing little to no data in the partially and fully developed boiling regimes. These measurements were conducted in a heated stainless-steel annulus over a range of pressures, velocities, and inlet subcoolings. The available tabulated dataset covers the full nucleate boiling regime up to CHF. The results show close agreement with the original MITB model validation presented by Kommajosyula [11].

Although CFD-integrated wall boiling models are beyond the scope of this study, the present 0D solver serves as a reduced-order assessment tool for identifying informative trends in wall-boiling model behavior across a broad range of conditions. By combining locally measured thermal inputs with bulk flow quantities from the experiments, the algebraic solver enables a consistent comparison of different wall boiling frameworks and closure combinations against experimental thermal data. In this way, the analysis provides useful guidance on the physical robustness and applicability of the evaluated modeling approaches for the CFD-oriented development. However, the present results should not be interpreted as a direct prescription for CFD implementation, since in 3D CFD, these closures act on local near-wall variables that may differ from the bulk quantities used here. Therefore, the application of the evaluated model combinations in CFD may require adaptation of the model inputs to local flow conditions near the wall.

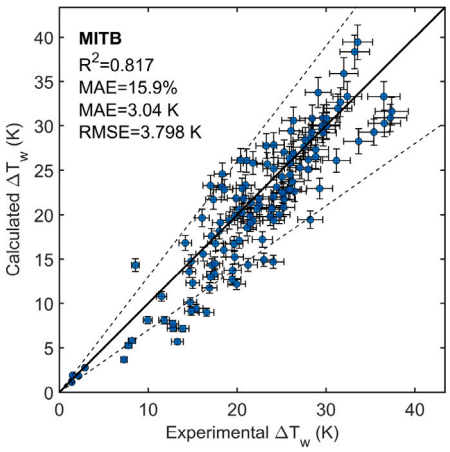

Fig. 1. Comparison between calculated and experimental wall superheats for Kennel experiments. Geometry: annulus, outer diameter $D = 10.67 - 19.56$ mm, heated length $L_{\mathrm{heat}} = 98$ mm. Flow conditions: $p = 0.2$–0.6 MPa, $G = 270$–$3500\ \mathrm{kg\,m^{-2}\,s^{-1}}$, $q'' = 0$–$6.5\ \mathrm{MW\,m^{-2}}$. Solid line: perfect agreement; dashed lines: ±30% bands.

3. Experimental data

3.1. Low pressure: Varava experiments

Varava et al.'s experimental campaign at the Moscow Power Engineering Institute provides a detailed dataset for fusion-relevant thermal-hydraulic conditions under one-sided heating [17,18]. These experiments were reported in both Varava's and Dedov's publications and were designed to recreate the convection and boiling heat transfer behavior of plasma-facing component cooling channels in the ITER thermonuclear reactor, particularly the divertor targets. The facility comprised a vacuum chamber, in which the horizontally oriented targets with coolant channels were heated by a scanning electron beam under conditions that yielded high heat fluxes characteristic of fusion-relevant operation. The experimental setup used both plain tubes and twisted-tape inserts. Table 1 summarizes flow parameters of the experimental campaign. The test sections used in the experimental campaign were: **TS1** (8.0 mm diameter, 14 mm heated length) with 0.50 mm tape thickness and twist ratio $y = 1.75$; **TS2** (8.0 mm diameter, 24 mm heated length) with 0.50 mm tape thickness and twist ratios $y = 1.75$, 2.4, 4.0, 6.3, and $y = \infty$ (plain); **TS3** (4.0 mm diameter, 20 mm heated length) with 0.35 mm tape thickness and twist ratios $y = 4.25$, 8.3, and $y = \infty$ (plain); and **TS4** (2.0 mm diameter, 20 mm heated length) with 0.35 mm tape thickness and twist ratio $y = 3.2$. Chromel–Alumel thermocouples were embedded at defined radial positions to measure the temperature field inside the target. Researchers applied a direct extrapolation method for wall temperature measurements. The reported uncertainties from the study were 5% for wall temperature, 8% for heat-flux density, and 10% for heat transfer coefficients, corresponding to approximately 10% uncertainty in wall superheat. In total, 336 data points were obtained using plot digitization across both single-phase and nucleate-boiling regimes. The dataset includes 199 data points for positive wall superheats, providing comprehensive coverage for model validation. As reported by Yagov and Varava, the Varava nucleate boiling experiments exhibited local CHF events without structural failure, which is typical for one-sided heating configurations [18,28]. In the present study, only data points below CHF are retained to ensure that the analysis is restricted to the pre-CHF nucleate boiling regime, which corresponds to 168 data points.

3.2. High pressure: Yan experiments

Yan et al. conducted experiments at the State Key Laboratory of Multiphase Flow in Power Engineering to investigate subcooled flow boiling under fusion-relevant thermal conditions [6,19]. The experimental facility utilized a vertical flow loop with electrically heated test sections to simulate uniform wall heating. Both plain and twisted-tape tubes with different twist ratios were tested. Table 1 summarizes the flow parameters of the experimental campaign. The test sections consisted of vertical nickel–alloy tubes with an inner diameter of 9.0 mm, wall thickness of 1.5 mm, and an effective heating length of 400 mm. Swirl-tape inserts with twist ratios of $y = 2$ and $y = 4$, while the plain configuration corresponded to $y = \infty$. K-type thermocouples were spot-welded along the outer wall at 50 mm intervals to measure the axial temperature distribution. The study reported heat-flux uncertainties of 4.9–6.4% and approximately 1% uncertainty in wall superheat. A total of 264 data points were collected using plot digitization, comprising 219 data points in the nucleate-boiling regime, which covers a wide range of flow and heat-flux conditions representative of fusion-relevant operations.

Table 1
Flow conditions of the experimental campaigns compared with fusion-relevant ranges.

Parameter	Fusion-relevant range	Varava	Yan
Pressure (MPa)	0.5–5	0.7–2.0	3.0–5.0
Mass flux ($kg\,m^{-2}\,s^{-1}$)	5000–20,000	340–25,000	6000–10,000
Subcooling (K)	10–200	111–189	29–203
Heat flux (MW/m^2)	0–50	0–50	5.0–19.5

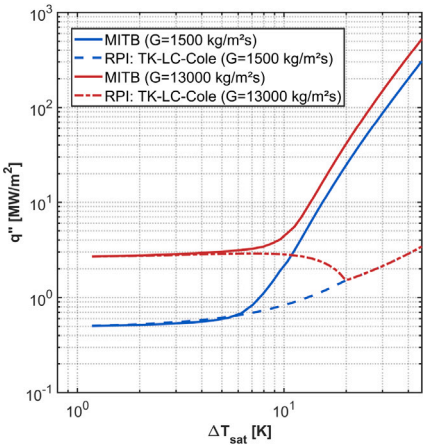

Fig. 2. Comparison of total heat flux q'' vs. wall superheat ΔT_{sat} for both *RPI* and *MITB* models at two mass fluxes: $G = 1500\ kg\,m^{-2}\,s^{-1}$ and $G = 13000\ kg\,m^{-2}\,s^{-1}$, in a smooth pipe at $p = 4$ MPa with subcooling of 30 K.

4. Investigation of bubble parameter models

As reported by Končar et al. [14], the RPI wall boiling model shows limitations under high mass-flux conditions. Fig. 2 compares the heat-flux responses of the RPI and MITB models under two mass-flux conditions. $G = 1500\ kg\,m^{-2}\,s^{-1}$ was used as a representative low mass flux for PWR-like conditions, and $G = 13,000\ kg\,m^{-2}\,s^{-1}$ for fusion-relevant high mass flux. At low mass flux, both models produce a monotonic increase of q'' with wall superheat ΔT_w. On the other hand, at high G, immediately after ONB, the RPI model produces a non-physical negative slope, $\partial q''/\partial \Delta T_w < 0$, whereas MITB maintains physically consistent behavior. The RPI model's behavior contradicts experimental trends [4,6,7,17] and the expected physics of flow boiling.

Končar [14] claimed that the issue might be rooted in the inherent quenching term of the RPI model. However, the RPI model also relies on boiling-parameter closure models, which can strongly influence its predictions. To investigate the applicability and limitations of the RPI model under high mass flux conditions, widely used closure models for bubble departure diameter, departure frequency, and nucleation-site density are examined in the following sections. More complex bubble-parameter models, which require local near-wall hydrodynamic information such as velocity gradients and thermal boundary layer profiles, are not considered here, as they fall outside the scope of the present 0D framework.

4.1. Bubble departure diameter models

During wall boiling, bubbles detach from the surface once they reach a characteristic departure diameter. Bubble departure diameter influences heat transfer components as well as other bubble parameters. In Table 2, the commonly used bubble departure diameter correlations are summarized. Tolubinsky and Kostanchuk [29] developed the TK model from high pressure water experiments, incorporating the influence of liquid subcooling, which plays a key role in determining bubble

Table 2
Bubble departure diameter correlations for subcooled flow boiling.

Model	Formulation	Applicable range
Tolubinsky–Kostanchuk (TK) [29]	$D_d = \min\left[0.0006 \exp\left(-\frac{\Delta T_{sub}}{45}\right), 0.0014\right]$	Water under PWR-type conditions.
Kocamustafaogullari (Koca) [30]	$D_d = 2.64 \times 10^{-5} \left(\frac{\sigma}{g\,\Delta\rho}\right)^{0.5} \left(\frac{\Delta\rho}{\rho_c}\right)^{0.9}$	$P_{sys} = 0.1–14.2$ MPa.
MITB (Komma)	$D_d = 18.9 \times 10^{-6} \left(\frac{\Delta\rho}{\rho_g}\right)^{0.27} \mathrm{Ja}_{sup}^{0.75} (1 + \mathrm{Ja}_{sub})^{-0.3} u_{liquid}^{-0.26}$, $\mathrm{Ja}_{sup} = \frac{\rho_f c_{pf} (T_{wall} - T_{sat})}{\rho_g h_{fg}}$, $\mathrm{Ja}_{sub} = \frac{\rho_f c_{pf} (T_{sat} - T_{liquid})}{\rho_g h_{fg}}$	$P = 0.1–13.8$ MPa, $u_f = 0.3–11.16$ m/s, $\Delta T_{sub} = 5–100$ K, $D_h = 6–15$ mm.

size. The TK model has been applied across a wide range of pressures, including fusion-relevant conditions [8,31–35]. Liu and Yu [13,36] used this model for divertor target simulations, while Colombo [37] reported that it tends to overpredict bubble diameters at elevated pressures.

Kocamustafaogullari [30] proposed a semi-mechanistic model (Koca) based on a force-balance formulation including gravity, surface tension, and pressure effects through density ratios. However, the model does not account for wall superheat, mass flux, or subcooling. Similar to the TK model, the Koca correlation has been widely adopted in subsequent studies [31,34,37–39].

Recently, Kommajosyula [11] introduced an empirical correlation (Komma), integrated within the MITB model. This correlation estimates the departure diameter using dimensionless parameters. The correlation includes the combined effects of pressure, subcooling, wall superheat, and bulk velocity.

4.1.1. Effect of bubble departure diameter models

In this investigation, only the departure-diameter correlation was varied to isolate the role of departure-diameter models in wall boiling predictions. Therefore, the nucleation-site density and departure-frequency submodels were fixed to Lemmert–Chawla and Cole, respectively (see Figs. 4 and 5). The same approach will be repeated for all bubble parameter model investigations. We investigated the RPI model with the TK, Koca, and Komma bubble parameter model combinations (Table 2), and the MITB model, comparing the predicted departure diameters and boiling curves with experimental measurements. For additional reference, the results were also compared against the CEA empirical correlation for nucleate boiling under fusion-relevant conditions (Thom–CEA correlation with the Rohsenow modification) [40].

Fig. 3 organizes these comparisons and links each predicted D_d trend (top) to its corresponding boiling curve (down): wall heat flux against wall superheat across four cases: high mass flux, low mass flux, low subcooling, and high pressure. The experimental measurements do not span the combined parametric space while holding other conditions fixed. Therefore, the Thom–CEA correlation is used as a general reference for high-pressure and low subcooling cases.

In the high-mass-flux case (a), With RPI model, Koca and Komma produce a nonphysical post-ONB drop in total heat flux q''; RPI–TK preserves a smooth trend but underpredicts the measurements over the examined superheat range. The heat-flux drop observed in the partially developed nucleate boiling region suggests the following mechanism: larger D_d increases the instantaneous active boiling area A_b, thereby suppressing the single-phase forced-convection contribution $\dot{q}_C$. This has been also demonstrated in the study of Koncar [14]. By contrast, MITB exhibits good agreement with the experiments, displaying physically consistent behavior.

At low mass flux case (b), convection is less dominant, so all RPI variants yield more physically consistent results. However, RPI predictions still lie below both the measurements and the empirical curve. This is consistent with the findings of Kommajosyula at similar mass fluxes [11]. In terms of departure-diameter response, TK and Koca show little sensitivity to G, while Komma exhibits a small systematic increase in D_d. Despite the larger D_d, RPI–Koca yields lower heat flux than RPI–Komma due to stronger convection suppression. This mentioned difference diminishes at higher wall superheat as the evaporation term becomes dominant.

Under low subcooling case (c), TK's explicit subcooling dependence gives larger D_d and produces a similar post-ONB heat-flux drop observed with the Koca and Komma models. This has important implications for the utilization of the TK model for fusion-relevant conditions. Some TK model implementations in CFD (e.g., in ANSYS) [22] use local fluid temperatures from near-wall cells, which are higher than the inlet bulk temperature; using these higher local temperatures further enlarges D_d and can extend unphysical behavior over a wider subcooling range when TK is coupled with RPI model. RPI–Koca and RPI–Komma show similar nonphysical responses, whereas MITB mimics the empirical trend with relative consistency.

At high pressure, as shown in (d), Koca and Komma predict smaller D_d, which may cause a more moderate drop in the convective and total heat flux in the PDNB regime. For MITB, the qualitative shape remains consistent with the empirical trend, but the model overpredicts heat flux. The high pressure and low subcooling lead to deviations from the Thom–CEA correlation, resulting in overpredicted heat fluxes.

Overall, the results in this section show that the RPI model exhibits unphysical heat-flux drops at higher wall superheats in the PDNB under high mass fluxes. The issue is not caused by the departure-diameter models themselves because the Komma model behaves physically within the MITB framework but not within RPI. These drops may arise from the RPI model's limited ability to compensate for the reduction in high convective heat transfers in high mass fluxes. This behavior is most evident at low subcooling for the TK model and at lower pressures for the Koca model. In contrast, the MITB model remains physically consistent and performs relatively better under the reported extreme mass-fluxes.

4.2. Bubble departure frequency models

The bubble departure frequency defines how often bubbles detach from the heated surface and consists of two components. First is the growth time, during which a bubble reaches its departure diameter. Second is the waiting time which represents the re-establishment of the thermal boundary layer before the next nucleation event. The majority of available departure frequency measurements were obtained at pressures below 0.5 MPa and under pool-boiling or low-mass-flux conditions, which are not representative of fusion-relevant flows. The models considered in this study are summarized in Table 3. Cole [41] proposed a frequency correlation based on photographic observations, assuming terminal rise velocity as the limiting condition. Cole model links departure frequency to the departure diameter and includes a density-ratio term, making it sensitive to pressure and bubble size. Although originally developed for pool boiling, it has been applied to subcooled flow boiling, including PWR and fusion-relevant conditions [8,13,32,38,43,44]. However, the model does not account for subcooling, wall superheat, or mass flux effects. Basu [42] addressed this by restructuring the departure frequency into growth and waiting time components, governed by wall superheat and subcooling. More recently, Kommajosyula [11] extended this partition approach, linking each timescale to parameters such as subcooling, wall superheat, and departure diameter. For the wait time, this was done by extending the empirical correlation using many experiments from the literature. And for the growth time, the bubble growth equations were used, combining the works of Cooper and Plesset [45,46].

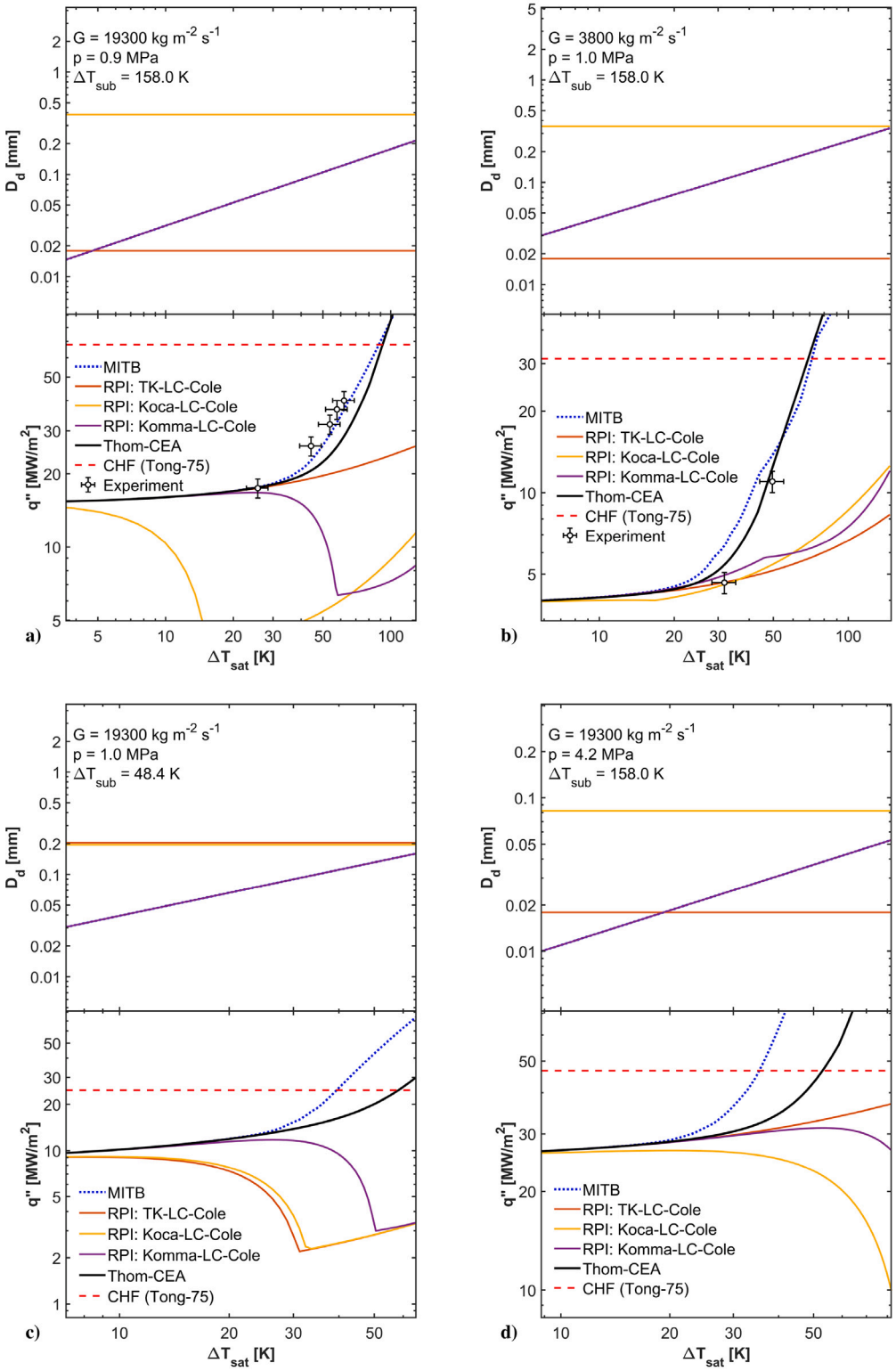

Fig. 3. Predicted boiling curves for different departure diameter models under various flow conditions for Varava TS3 geometry with a smooth plain tube: (a) high mass flux; (b) low mass flux; (c) low subcooling; (d) high pressure. MITB and RPI with the Komma departure diameter model intersect in all cases.

4.3. Effect of departure frequency models

Fig. 4 shows a general comparison of the predictions of the RPI model with different departure frequency models and the complete MITB model. Similar to the previous section, the results are compared with the Varava measurements and the Thom–CEA correlation.

For the high-mass-flux case (a), both RPI–Cole and RPI–MITB frequency models preserve a physically consistent boiling-curve trend but underpredict the experimental heat fluxes across the examined superheat range. The RPI–Basu model shows closer agreement but exhibits unrealistically high departure frequencies due to its strong dependence on wall superheat, a consequence of being calibrated under lower

Table 3
Bubble departure frequency correlations for subcooled flow boiling.

Model	Formulation	Applicable range
Cole [41]	$f_d = \sqrt{\frac{4}{3}\frac{g(\rho_l-\rho_v)}{\rho_l D_b}}$	Pool boiling near CHF.
Basu et al. [42]	$f_d = \frac{1}{t_{\text{growth}} + t_{\text{wait}}}$, $\frac{D_b^2}{\eta_l \text{Ja}_{\text{sup}} t_g} = 45\exp(-0.02\,\text{Ja}_{\text{sub}})$, $t_w = 139.1\,(\Delta T_w)^{-4.1}$	Subcooled flow boiling. $G = 235$–684 kg m^{-2} s^{-1}, $q'' = 200$–454 kW m^{-2}, $\Delta T_{\text{sub}} = 7.7$–$46.5$ K.
Kommajosyula (MITB) [11]	$t_{\text{wait}} = \frac{0.0061\,\text{Ja}_{\text{sub}}^{0.63}}{\Delta T_{\text{sup}}}$, $t_{\text{growth}} = \left(\frac{D_d}{2K}\right)^2$, $K = \text{Ja}_{\text{sup}}\sqrt{\eta_f}\left[\frac{1.243}{\sqrt{\text{Pr}_f}} - \min\left(0.5\,\frac{1.243}{\sqrt{\text{Pr}_f}}, 0.0977\,\frac{T_{\text{sub}}}{T_{\text{sup}}}\right)\right]$	Validated for water over: $P = 0.1$–13.8 MPa, $u = 0.3$–11.16 m/s, $\Delta T_{\text{sub}} = 5$–$100$ K, $D_h = 6$–15 mm.

Table 4
Nucleation site density correlations for subcooled flow boiling.

Model	Formulation	Applicable range
Lemmert–Chawla (LC) [47]	$N_a = (210\,\Delta T_w)^{1.805}$	$P_{\text{sys}} = 101$ kPa.
Basu et al. [48]	$N_a = \begin{cases} 0.34(1-\cos\theta)\,\Delta T_w^{2.0}, & \Delta T_w < 15\text{ K} \\ 3.4\times10^{-1}(1-\cos\theta)\,\Delta T_w^{5.3}, & \Delta T_w \geq 15\text{ K} \end{cases}$	ΔT_w : 3–26.5 K, θ : 30–90°.
Hibiki–Ishii (HI) [49]	$N_a = \tilde{N}_a\,[1-\exp(-\frac{\theta^2}{8\mu^2})]\left\{\exp\left[f(\rho^+)\frac{l'}{R_c}\right]-1\right\}$, $f(\rho^+) = -0.01064 + 0.48246\rho^+ - 0.22712(\rho^+)^2 + 0.05468(\rho^+)^3$, $\rho^+ = \ln\left(\frac{\rho_l-\rho_g}{\rho_g}\right)$, $R_c = \frac{2\sigma[1+(\rho_g/\rho_l)]/P_l}{\exp\left[\frac{h_{lg}(T_g-T_{\text{sat}})}{RT_gT_{\text{sat}}}\right]-1}$.	$G = 0$–886 kg m^{-2} s^{-1}, $P_{\text{sys}} = 0.101$–19.8 MPa, $\theta = 5$–$90°$, $N_a = 10^4$–10^{10} sites m^{-2}.
Modified Hibiki–Ishii (MHI, Gilman [10])	$N_a = \begin{cases} N_{\text{HI}}, & \Pi < e^{-1}, \\ \frac{0.2689\,\Pi + 0.2690}{N_0}, & e^{-1} \leq \Pi < e, \\ \frac{\ln\Pi - \ln(\ln\Pi)}{N_0}, & \Pi \geq e, \end{cases}$ $\Pi = N_0 N_{\text{HI}}$, $N_0 = f_d\,t_{\text{growth}}\pi(D_d/2)^2$	Extension of HI. $P = 0.1$–13.8 MPa, $u_f = 0.3$–11.16 m/s, $\Delta T_{\text{sub}} = 5$–$100$ K, $D_h = 6$–15 mm.

superheat conditions. The full MITB model, which uses its native MITB frequency formulation, agrees well with the measurements, indicating that the discrepancies in the RPI–MITB configuration are not caused by the frequency submodel itself.

At low mass flux (b), the MITB model continues to reproduce consistent heat-flux trends, whereas the RPI–Basu model again yields excessive frequencies.

Under low subcooling (c), larger departure diameters enlarge the bubble-influenced area and induce a post-ONB convective heat-flux drop, consistent with the earlier analysis on the departure diameter section. The MITB model follows a more physically consistent trend with realistic frequency predictions but overpredicts heat flux at low subcooling.

At high pressure (d), the MITB model retains qualitative agreement with the empirical correlation but tends to overpredict the heat flux.

Similar to the departure diameter investigation, the results indicate that the RPI framework tends to produce lower heat fluxes and unphysical behavior under extreme mass fluxes and low subcooling in the PDNB. These inconsistencies seem to originate from limitations in the RPI formulation or other bubble parameters models rather than the departure-frequency models themselves. While the Basu model improves apparent agreement, it does so by yielding unrealistically high frequencies.

4.4. Nucleation site density models

Active nucleation site density is the number of bubble nucleation sites formed per area on the wall. Various mechanistic and empirical correlations, commonly used in pressurized water reactor conditions, are listed in Table 4.

It is well established that the nucleation site density depends strongly on wall superheat, which is commonly expressed as a power-law relationship. Lemmert and Chawla (LC) [47] demonstrated this correlation, as shown in Table 4. However, at higher pressures and across wider wall-superheat ranges, the LC formulation may not be ideal to use, necessitating case-specific tuning [31,43]. Although originally developed outside the fusion-relevant regime, the LC model has been attempted to be applied in several fusion-relevant cases [36,44]. Basu et al. [48] created an empirical correlation based on experiments with different contact angles. Basu et al. also show that the power relationship between wall superheat and nucleation density is not constant but changes with the superheat itself. However, the Basu model is not pressure-sensitive as it was created under atmospheric conditions. Hibiki and Ishii (HI) further addressed this by introducing a semi-mechanistic model for nucleation site density, emphasizing the exponential relationship between nucleation site density and parameters such as wall superheat and pressure [49]. This model considers pressure effects, wall superheat, and contact angle. Gilman [10] noted that the HI model frequently predicts unrealistically high numbers of active nucleation sites due to its exponential relationship with wall superheat, which is particularly evident for high wall superheats. To address these discrepancies, Gilman proposed a refined approach that distinguishes between the actual number of active bubbles forming on the heater surface and the potential nucleation sites where bubbles could form. In this modified Hibiki–Ishii model (MHI) once a critical number of nucleation sites is reached, additional activation does not result in increased bubble formation due to spatial limitations on the surface.

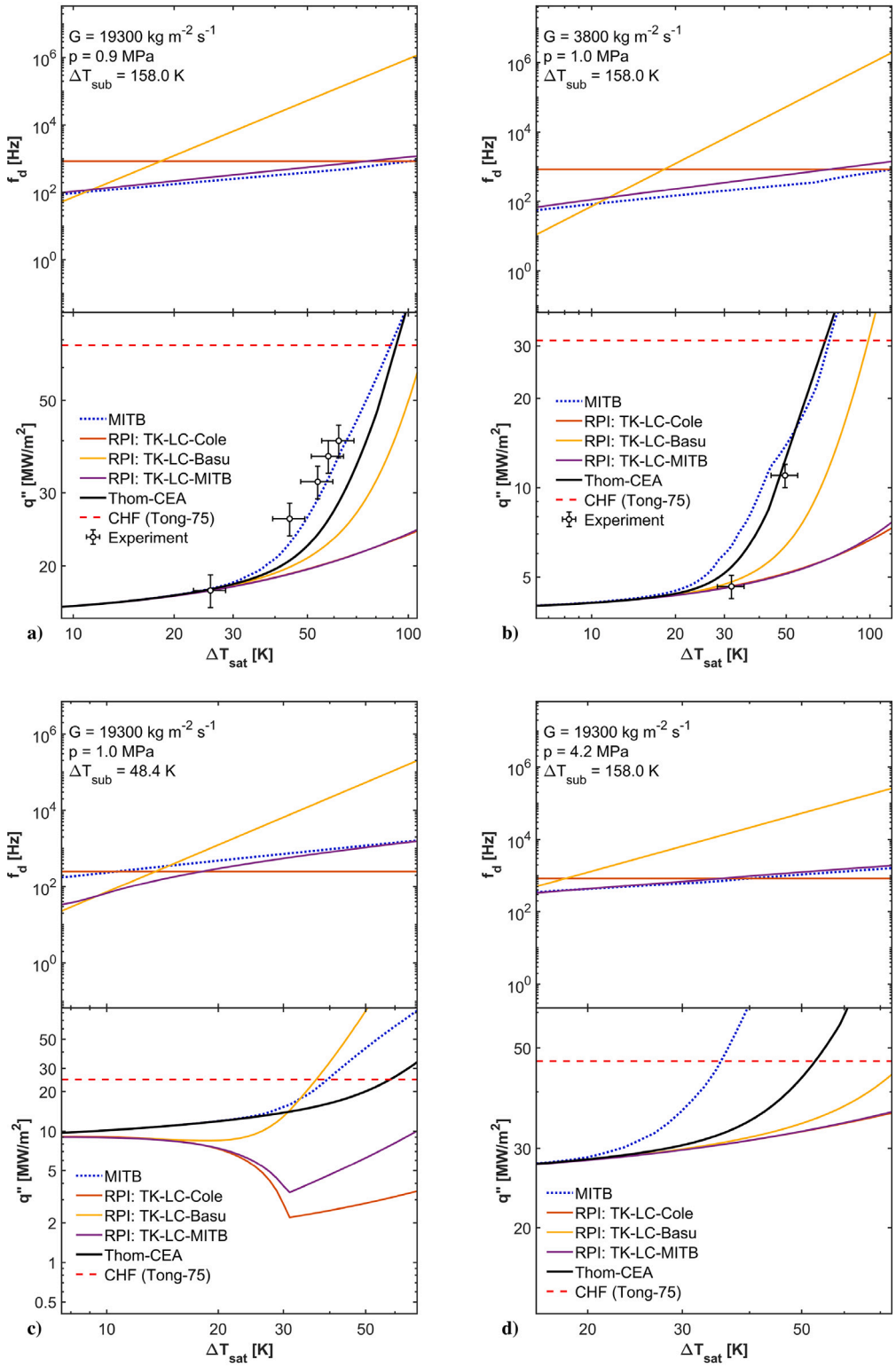

Fig. 4. Predicted boiling curves and bubble departure frequency parameters under different flow conditions for Varava TS3 geometry with a smooth plain tube: (a) high mass flux; (b) low mass flux; (c) low subcooling; (d) high pressure.

4.5. Effect of nucleation site models

In Fig. 5, at high mass flux, (a) all RPI configurations under-predict the measured heat fluxes. While higher nucleation-site densities might be expected to mitigate this problem, similar to the effect of larger diameters in the previous section, they instead intensify the drop in heat flux in the PDNB region by expanding the active boiling area. In the low-mass-flux case (b), contributions from convection become less pronounced, thus, all RPI models provide more physically consistent results. In these circumstances, increasing site density improves agreement, especially for the RPI-MHI models. Under low subcooling, (c), large bubble sizes caused by TK significantly increase heat flux

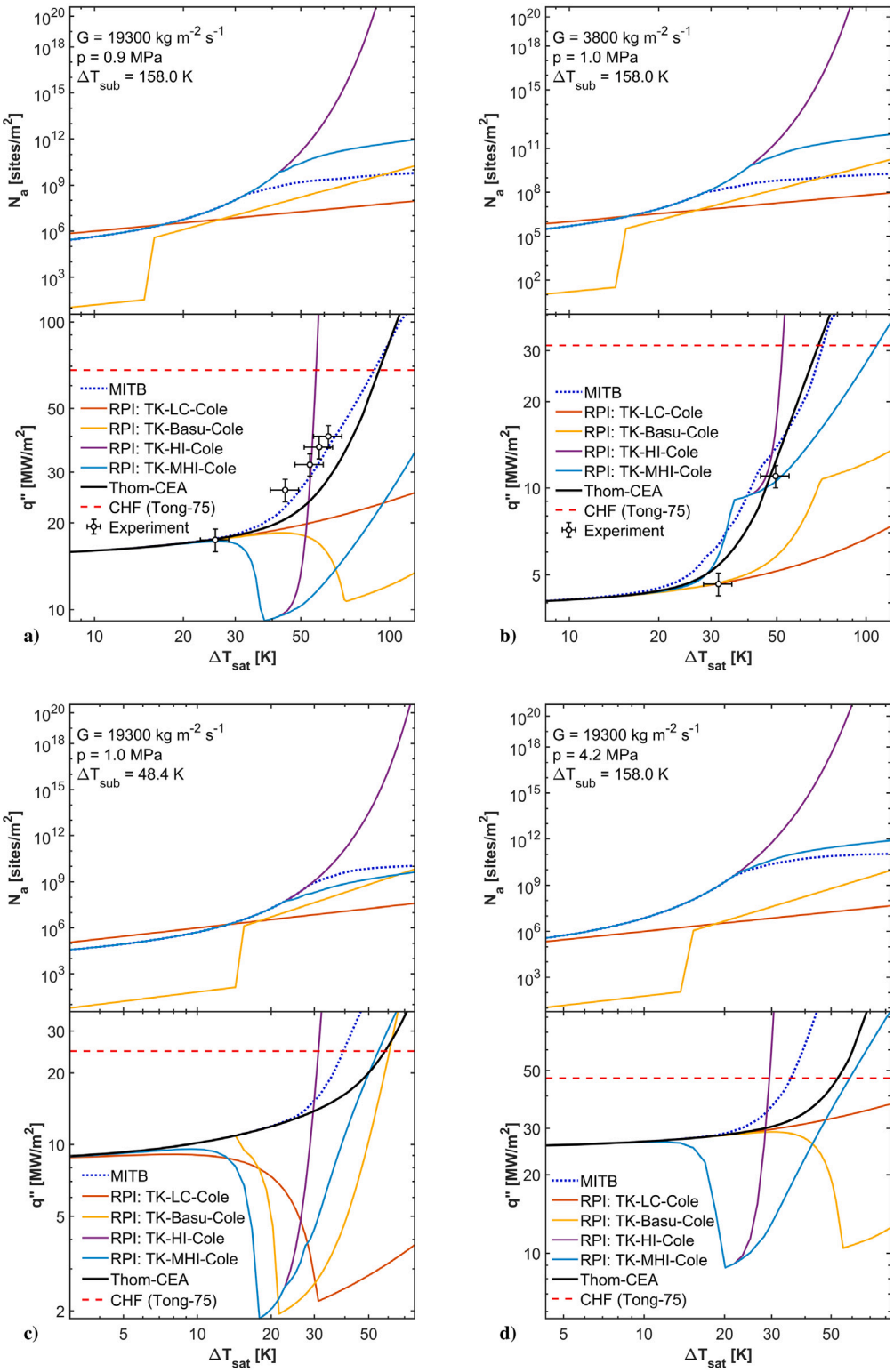

Fig. 5. Predicted boiling curves and nucleation site density parameters under different flow conditions for Varava test Section 3 geometry with a smooth plain tube: (a) high mass flux; (b) low mass flux; (c) low subcooling; (d) high pressure.

drop in combination with large site densities. In the FDNB region, results from both the Basu and MHI models improve agreement with the experiments. The MITB model reproduces the general experimental trends with physically coherent behavior; however, at high pressure (d), it overpredicts the heat flux.

Overall, the LC model fails to capture the increase in nucleation-site density at high wall superheats, leading to underpredicted heat fluxes. The original Hibiki–Ishii (HI) model, in contrast, produces unrealistically high site densities due to its exponential dependence on wall superheat, resulting in excessive heat fluxes at high superheats that

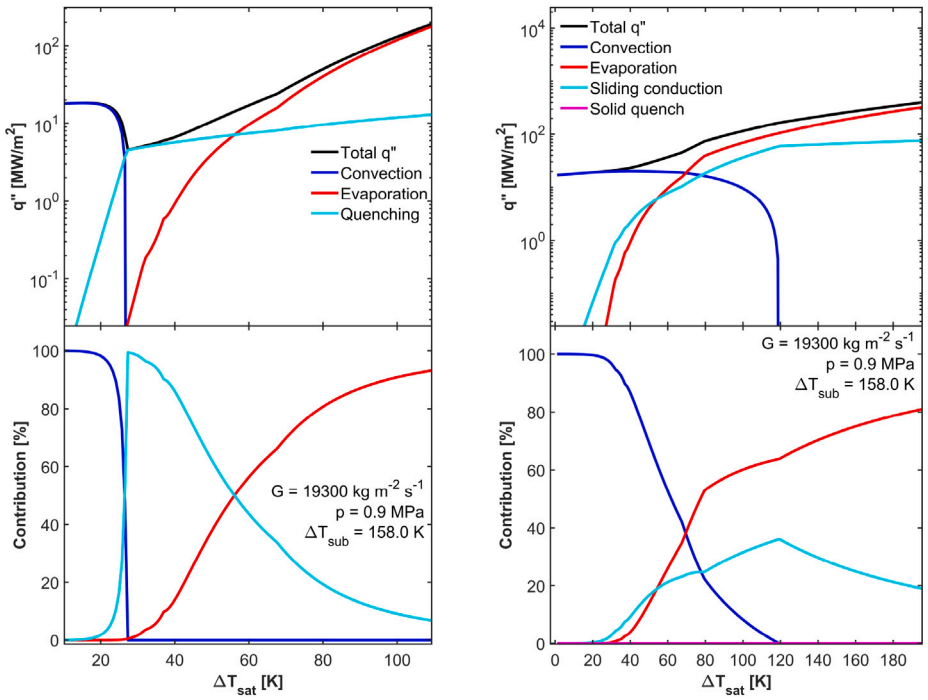

Fig. 6. Partitioning of the wall heat flux into individual heat-transfer terms shown as absolute heat fluxes for a smooth tube at $G = 19,300\ \mathrm{kg\,m^{-2}\,s^{-1}}$, $p = 0.9$ MPa, and $\Delta T_{\mathrm{sub}} = 158.0$ K. Left: RPI model with MITB (Komma–MHI–MITB) bubble-parameter models. Right: MITB model.

deviate from experimental measurements. Hence, the LC and Hibiki–Ishii models are not suitable to calculate site density values relevant to fusion flow conditions without further modifications. The modified Hibiki–Ishii (MHI) model provides more balanced results due to its suppression mechanism, providing physically consistent predictions over a wider superheat range and improved agreement with empirical correlations. In general, independent of the site density models, the RPI model again yields nonphysical boiling curves in the PDNB region at high mass fluxes. While at FDNB, the RPI-MHI model yields promising results. MITB model, on the other hand, may be more suitable for high heat and mass flux conditions like fusion-relevant conditions.

5. Investigation of wall boiling models

5.1. Heat partition analysis

In this section, the inherent issues suggested in the previous section are analyzed through a detailed investigation of heat partitioning in the RPI and MITB wall boiling models. The influence of the heat-partitioning formulation is assessed by comparing the heat-flux components of the RPI model that uses MITB bubble parameter models to those of the complete MITB model.

As shown in Fig. 6, the RPI model predicts a decrease in total heat flux once the wall superheat exceeds the saturation temperature. This behavior is physically inconsistent, as flow boiling should enhance wall heat transfer and thereby increase heat removal rather than reduce it. The present results indicate that this non-physical behavior arises from the combined effect of the $(1 - A_b)$ formulation and the inconsistent response of the quenching term. As discussed in Section 4, the expansion of the bubble-influenced area, A_b, suppresses the single-phase forced-convection contribution through the $(1 - A_b)$ factor. As A_b approaches unity, the convective term vanishes regardless of the magnitude of h_c, leaving the quenching term as the sole wall-to-liquid heat-transfer contribution. Since the quenching term in the RPI framework does not scale with mass flux, it produces a non-physical reduction in total heat flux under fusion-relevant conditions until the evaporation term becomes sufficiently large to compensate for this deficiency at higher wall superheats. Although the evaporation term increases sharply at higher wall superheats, this delayed rise only partially restores the total heat flux. Higher nucleation-site densities intensify evaporation at large wall superheats, but further suppress convection at lower ones. It should also be noted that the present analysis is based on a 0D model. In CFD models with a coupled flow field, bubble-induced turbulence may enhance the effective near-wall heat-transfer coefficient and thus reduce the severity of the predicted negative slope. However, as A_b approaches unity, the convective term vanishes irrespective of the h_c value, and since the quenching term does not increase with mass flux, the non-physical drop of total heat flux remains.

On the other hand, Fig. 6 presents that in the MITB model, the suppression of convection is moderate relative to the RPI model. This may be due to the calculation of convection suppression by the time-averaged sliding coverage area, which accounts for the bubble growth duration fraction. In addition, the sliding-conduction term scales with the forced-convection heat-transfer coefficient through the semi-infinite boundary-reestablishment approximation. These features produce a more physical, smoother convection decay and a mass flux-dependent increase in boiling-induced heat transfer.

5.2. Model evaluation

Here, three different wall boiling models are compared against extensive experimental datasets from fusion-relevant high-mass- and high-heat-flux experiments. The standard RPI model, (RPI: TK–LC–Cole) is compared with the MITB model. Additionally, an RPI model variant employing the Koca departure-diameter model, the Modified Hibiki–Ishii nucleation model, and the Cole frequency correlation is evaluated due to its thermal prediction performance improvements in the FDNB regime. Fig. 7 shows the comparison of predicted and experimental wall superheat for the Yan and Varava dataset. The comparison is done utilizing three statistical metrics: the coefficient of determination (R^2), which measures correlation strength, and the Mean Absolute Error (MAE) and Root Mean Squared Error (RMSE), which are used to assess accuracy. The dataset has 387 data points in the PDNB and FDNB regions, encompassing a broad range of flow conditions. The

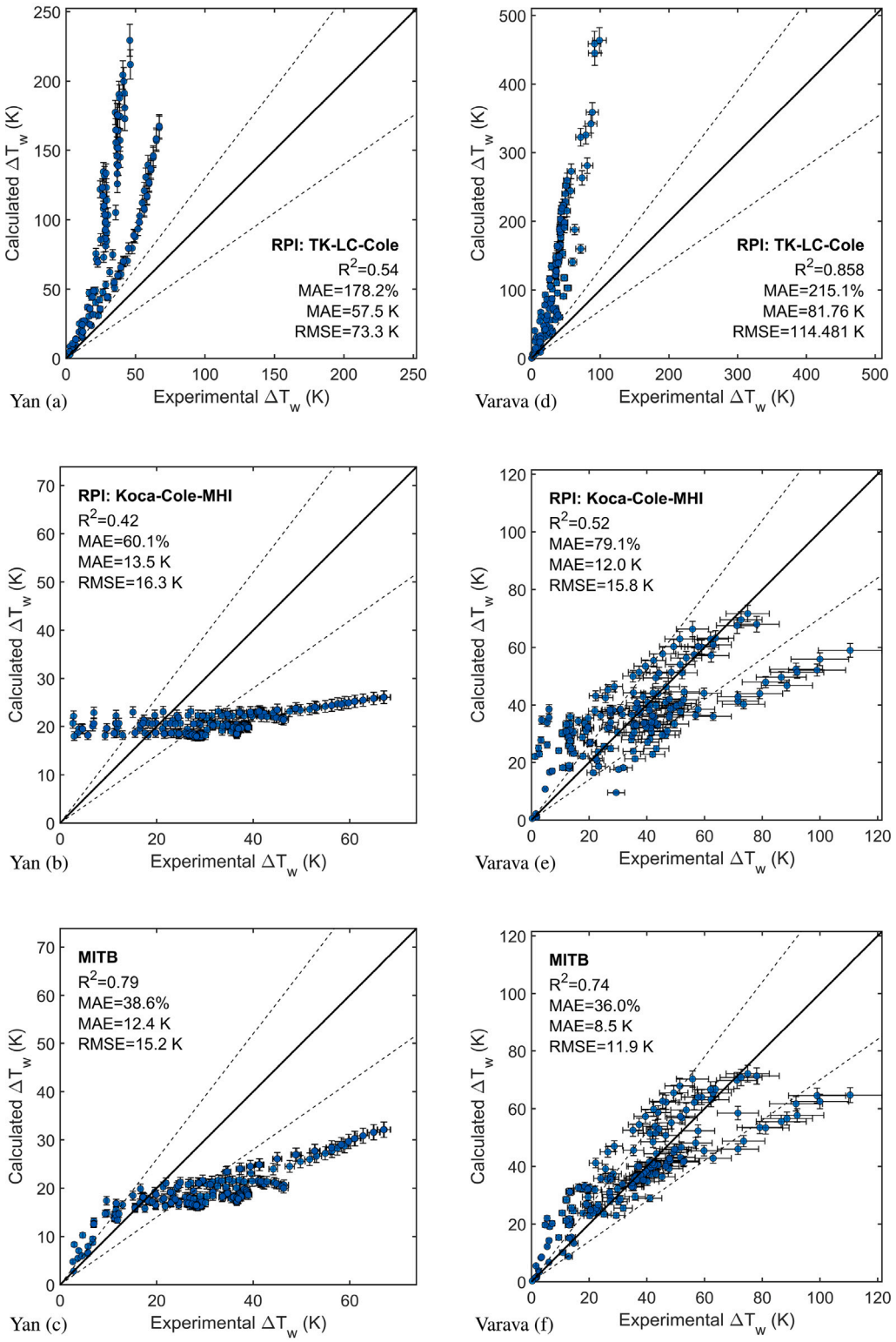

Fig. 7. Comparison between calculated and measured wall superheats using different wall boiling model combinations for the experiments of Yan (a–c) and Varava (d–f). **Yan geometry:** smooth tube and swirl-tape insert, D = 9.0 mm, L_{heat} = 400 mm, twist ratio y = 2–4 (plain $y = \infty$). **Yan flow:** p = 3.0–5.0 MPa, G = 6,000–10,000 kg m^{-2} s^{-1}, T_{in} = 50–200 °C, q'' = 5.0–19.5 MW m^{-2}. **Varava geometry:** smooth tube and swirl-tape insert, D = 2.0–10.0 mm, L_{heat} = 14–24 mm, twist ratio y = 1.75–8.3 (plain $y = \infty$). **Varava flow:** p = 0.7–2.0 MPa, G = 340–25,000 kg m^{-2} s^{-1}, T_{in} = 15–60 °C, q'' = 0–50.0 MW m^{-2}. Solid line: perfect agreement; dashed lines: ±30% bands.

uncertainties are taken from the experiments, and the uncertainty in the calculated wall superheat is propagated from the input measured heat flux. To isolate the performance of the wall boiling submodels, single-phase heat transfer coefficients are taken directly from the experiments. For comparison, the MITB model is also evaluated with the Gnielinski single-phase correlation to assess its influence on the overall predictions.

The standard RPI model predicts extremely high wall superheats ($MAE = +58\ K, +82\ K$) and ($RMSE = +73\ K, +114\ K$) for the Yan and Varava experiments across a wide range of flow conditions. This behavior is mainly caused by the low nucleation-site density predicted by the LC model and the RPI model's suppression of the convection term and insufficient quenching.

When the RPI heat partition framework is used with alternative bubble-parameter models (Koca-MHI-Cole), the issue is partially mitigated at FDNB region due to the MHI model. However, the inherent convection-suppression problem of the RPI formulation remains, still resulting in high wall-superheat predictions at the PDNB region. On the other hand, in the FDNB region at very high wall superheats, the alternative RPI configuration tends to underpredict the wall superheat. Overall, RPI: Koca-MHI-Cole model offers relatively improved errors, although its trend ($R^2 = 0.42$) and ($R^2 = 0.54$) deviates from the experimental behavior for Yan and Varava, respectively.

The MITB model addresses the overprediction of wall superheats through its sliding-conduction formulation. The MITB model demonstrates substantial improvement in accuracy compared to the generic RPI model.

Fig. 8 illustrates the influence of applying the Gnielinski correlation for single-phase heat transfer within the MITB model on Nusselt number predictions for the Yan and Varava datasets. The inclusion of the single-phase correlation leads to only a marginal reduction in prediction accuracy. Overall, the MITB model coupled with the Gnielinski correlation provides improved heat-transfer predictions compared with the other wall boiling models considered.

5.3. Parametric analysis of MITB model

In this section, a parametric analysis is performed to quantify the influence of flow and geometric parameters on the thermal prediction accuracy of the MITB model in the nucleate boiling regime. The effects of heat-flux distribution, geometric parameters, subcooling, mass flux, heat flux, and pressure are investigated. Prediction errors are evaluated using the Nusselt number, which is calculated for each data point and compared to the corresponding experimental value. For each parameter, the data are grouped into parameter intervals, and the mean percentage error within each interval is reported together with the corresponding standard deviation, as shown in Fig. 9.

Figs. 9 and 10 (a) & (b) summarizes the influence of flow parameters on model accuracy. Variations in mass flux do not lead to significant changes in prediction error. In contrast, a deterioration in prediction accuracy is observed at higher pressures and lower subcooling levels. These trends are consistent with the observations reported in Section 4. Under high-pressure and low-subcooling conditions, the MITB model tends to predict lower HTCs at the PDNB region and higher at the FDNB region. A possible explanation for this deviation may be associated with the bubble departure diameter correlation employed in the MITB model. The Kommajosyula correlation is largely empirical, and its high-pressure calibration relies primarily on saturated pool boiling data. Under high-pressure and low-subcooling conditions, this may lead to overpredicted departure diameters, which can increase the sliding coverage area and enhance the suppression of the convective contribution in the PDNB region, while later leading to excessive evaporation in the FDNB region. Further calibration of the bubble departure diameter correlation against subcooled flow boiling data at high pressures may improve the accuracy of the MITB model under these conditions.

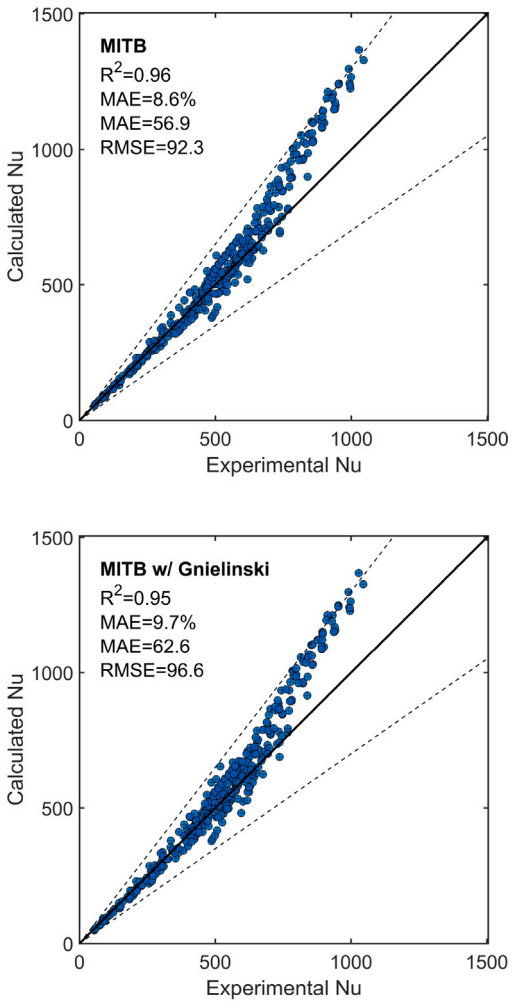

Fig. 8. Comparison between calculated and measured Nusselt numbers for the MITB model without (a) and with (b) the Gnielinski single-phase correlation for the complete dataset.

The effects of heat-flux magnitude and heat-flux distribution are shown in Fig. 10 (c) and (d). The prediction accuracy shows only a mild dependence on whether the heating is uniform or one-sided. The higher errors observed for uniformly heated cases are primarily attributed to the Yan dataset, which is characterized by higher pressure conditions. Overall, it can be said that heat-flux distribution does not have a significant impact on model performance. In addition, no systematic trend in prediction error is observed with increasing local heat flux. Consequently, the MITB provides comparable accuracy across the investigated heat-flux ranges and heating configurations.

Fig. 10 (e) and (f) show the influence of geometric parameters on model accuracy. A moderate increase in prediction error is observed with increasing length-to-diameter ratio. Since the flow is fully developed in these experiments, this trend may be associated with increased vapor generation over longer heated lengths, which can enhance non-local effects and geometric sensitivities not explicitly represented in the model. In contrast, no significant variation in prediction error is observed with changes in twist ratio or when comparing swirl-tape geometries with smooth tubes. Although improved agreement might be expected for smooth tubes, the comparable error levels indicate that the swirl-induced modifications to the effective velocity are adequately captured by the applied swirl corrections.

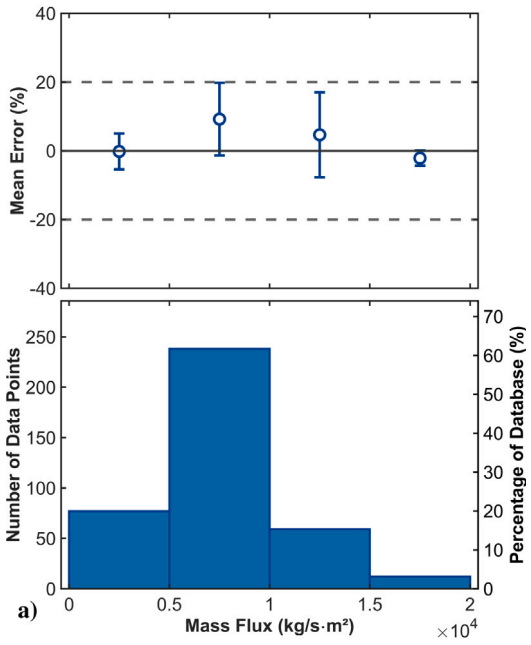

Fig. 9. Distribution of Varava and Yan database together with the mean error of Nusselt number prediction and corresponding standard deviation for the MITB model, presented as a function of mass flux.

6. Conclusion

Based on the comprehensive investigation of wall boiling models under fusion-relevant high-mass- and high-heat-flux conditions, the following conclusions can be drawn:

1. **The RPI heat-partitioning framework is inherently unsuitable for fusion-relevant high-mass-flux conditions.**
   Under extreme mass fluxes ($G > 4000\ \mathrm{kg\,m^{-2}\,s^{-1}}$), the RPI model yields an unphysical decline in heat flux with increasing wall superheat in the PDNB regime. The quenching term does not scale with mass flux and therefore cannot compensate when the elevated convective heat-transfer term is suppressed by the expansion of the bubble-influenced area.
2. **Prediction errors at high wall superheats are strongly influenced by the nucleation site density model.**
   At extreme wall superheats, an unsuitable nucleation site density model can cause large heat-flux errors even in the FDNB regime. The Lemmert–Chawla model severely underpredicts, while the original Hibiki–Ishii diverges exponentially at high wall superheats. The Modified Hibiki–Ishii correlation appears to be the most suitable candidate for fusion conditions.
3. **Boiling-parameter selection cannot overcome the limitations of the RPI framework.**
   While bubble-parameter model combinations such as Koca–MHI–Cole improve the prediction performance of the RPI model in the FDNB regime, they fail to resolve the issues in the PDNB regime. The bubble-parameter models that behave physically within the MITB framework but not within RPI indicate that the limitation originates from the heat-partitioning formulation rather than the bubble correlations themselves.
4. **The MITB heat partitioning framework captures more governing mechanisms through mass-flux-dependent terms.**
   The use of a convection-scaled sliding-conduction formulation, combined with time-averaged bubble coverage, enables smooth transition from PDNB to FDNB without heat-flux drops. This physics-based approach lowers prediction errors and yields more physically consistent results than the RPI model.
5. **The MITB model demonstrates applicability to fusion-relevant high-mass-flux conditions with further improvement.**
   Although the MITB model significantly improves predictive agreement, deviations observed under high-pressure and low-subcooling conditions highlight opportunities for targeted calibration and refinement.
6. **Critical experimental validation gaps remain.**
   The current validation is limited to wall temperature measurements, as experimental data on boiling quantities, such as nucleation site density, bubble departure characteristics, and void fraction distributions, are not yet available under fusion-relevant conditions. Consequently, the mechanistic interpretations proposed here are physically motivated by the heat-partitioning analysis and consistency with the wall temperature trends, but they cannot yet be directly confirmed by dedicated measurements of boiling behavior. Availability of such data would both improve the assessment of prediction accuracy and enable a more rigorous basis for testing the physical interpretations made in this study. Future measurements of these quantities are therefore essential to further validate wall boiling models and to strengthen the physical basis of heat-flux partitioning at extreme flow conditions.

CRediT authorship contribution statement

Ahmet Kılavuz: Writing – review & editing, Writing – original draft, Visualization, Validation, Software, Methodology, Investigation, Formal analysis, Data curation. **Boštjan Koncar:** Writing – review & editing, Supervision, Conceptualization. **Jeong-Ha You:** Writing – review & editing, Supervision, Resources, Conceptualization. **Rudolf Neu:** Writing – review & editing, Supervision, Resources.

Declaration of generative AI and AI-assisted technologies in the manuscript preparation process

During the preparation of this work, the original draft author used *ChatGPT* to assist with language editing and clarity improvements. After using this tool, the author(s) carefully reviewed and edited the content as needed and take(s) full responsibility for the content of the published article.

Declaration of competing interest

The authors declare the following financial interests/personal relationships which may be considered as potential competing interests: Rudolf Neu is Editor-in-Chief of Fusion Engineering and Design. Given his editorial role, he had no involvement in the peer-review of this article and had no access to information regarding its peer-review. Full responsibility for the editorial process for this article was delegated to another journal editor. If there are other authors, they declare that they have no known competing financial interests or personal relationships that could have appeared to influence the work reported in this paper.

Acknowledgments

This research was conducted within the framework of the EUROfusion Consortium, funded by the European Union under the Euratom Research and Training Programme (Grant Agreement No. 101052200 — EUROfusion). The views and opinions expressed are solely those of the author(s) and do not necessarily represent those of the European Union or the European Commission. Neither the European Union nor the European Commission can be held responsible for them.

The financial support provided by the Slovenian Research Agency through grants P2–0026 and P2–0405 is gratefully acknowledged.

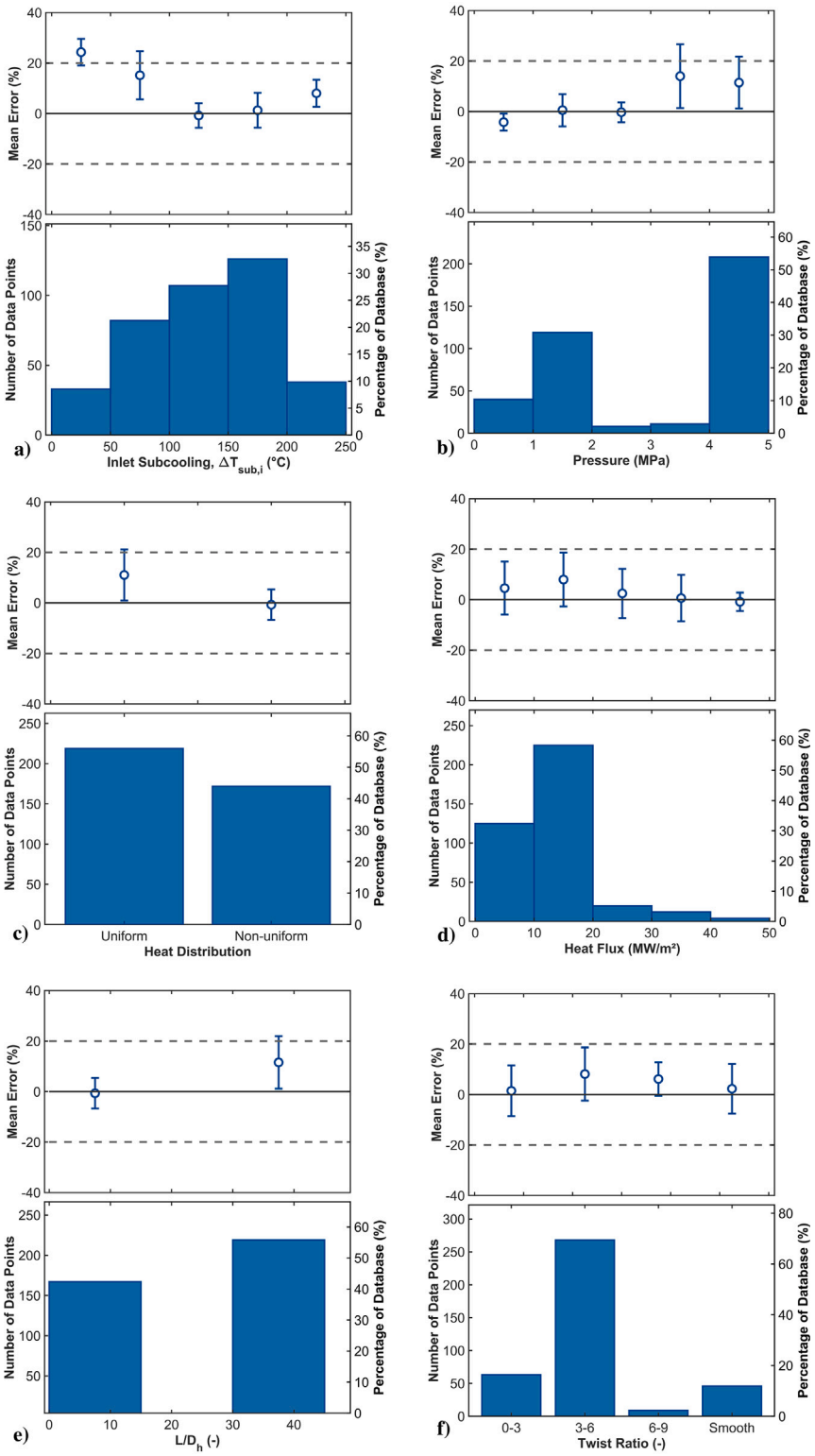

Fig. 10. Distribution of Varava and Yan database together with the mean error of Nusselt number prediction and corresponding standard deviation for the MITB model, presented as functions of: (a) subcooling; (b) pressure; (c) heat load uniformity; (d) heat flux; (e) length-to-diameter ratio; (f) twist ratio.

Data availability

Data will be made available on request.

References

[1] J.H. You, G. Mazzone, E. Visca, H. Greuner, M. Fursdon, Y. Addab, C. Bachmann, T. Barrett, U. Bonavolontà, B. Böswirth, F.M. Castrovinci, C. Carelli, D. Coccorese, R. Coppola, F. Crescenzi, G. Di Gironimo, P.A.D. Maio, G. Di Mambro, F. Domptail, D. Dongiovanni, G. Dose, D. Flammini, L. Forest, P. Frosi, F. Gallay, B.E. Ghidersa, C. Harrington, K. Hunger, V. Imbriani, M. Li, A. Lukenskas, A.

Maffucci, N. Mantel, D. Marzullo, T. Minniti, A.V. Müller, S. Noce, M.T. Porfiri, A. Quartararo, M. Richou, S. Roccella, D. Terentyev, A. Tincani, E. Vallone, S. Ventre, R. Villari, F. Villone, C. Vorpahl, K. Zhang, Divertor of the European DEMO: Engineering and technologies for power exhaust, Fusion Eng. Des. 175 (2022) http://dx.doi.org/10.1016/j.fusengdes.2022.113010.

[2] P.A. Di Maio, I. Catanzaro, G. Bongiovì, F.M. Castrovinci, P. Chiovaro, S. Giambrone, A. Gioè, F.A. Hernández, I. Moscato, G.A. Spagnuolo, A. Quartararo, E. Vallone, Thermofluid-dynamic and thermal–structural assessment of the EU-DEMO WCLL "double bundle" breeding blanket concept left outboard segment, Fusion Eng. Des. 202 (2024) 114335, http://dx.doi.org/10.1016/j.fusengdes.2024.114335.

[3] F.M. Castrovinci, A. Quartararo, S. Basile, G. Bongiovì, R. Burlon, P. Chiovaro, P.A. Di Maio, A. Gioè, S. Maggio, G. Mazzone, E. Tomarchio, S. Vacca, E. Vallone, J.-H. You, Thermofluid-dynamic assessment of the dual cooling scheme EU-DEMO divertor cassette, Fusion Eng. Des. 214 (2025) 114903, http://dx.doi.org/10.1016/j.fusengdes.2025.114903.

[4] M. Araki, M. Ogawa, T. Kunugi, K. Satoh, S. Suzuki, Experiments on heat transfer of smooth and swirl tubes under one-sided heating conditions, Int. J. Heat Mass Transfer 39 (1996) 3045–3055.

[5] J. Schlosser, J. Boscary, Finite elements calculations for plasma facing components, in: Proceedings of Specialist Workshop on High Heat Flux Component Cooling, vol. 18, Grenoble, 1993.

[6] J. Yan, Q. Bi, L. Cai, G. Zhu, Q. Yuan, Subcooled flow boiling heat transfer of water in circular tubes with twisted-tape inserts under high heat fluxes, Exp. Therm. Fluid Sci. 68 (2015) 11–21, http://dx.doi.org/10.1016/j.expthermflusci.2015.04.003.

[7] G. Zhu, Q. Bi, L. Cai, J. Yan, H. Lv, Subcooled flow boiling heat transfer of water in a circular channel with a twisted tape insert under high and non-uniform heat fluxes, Appl. Therm. Eng. 138 (2018) 722–730, http://dx.doi.org/10.1016/j.applthermaleng.2018.04.040.

[8] E. Krepper, B. Končar, Y. Egorov, CFD modelling of subcooled boiling—Concept, validation and application to fuel assembly design, Nucl. Eng. Des. 237 (7) (2007) 716–731, http://dx.doi.org/10.1016/j.nucengdes.2006.10.023.

[9] N. Kurul, M. Podowski, Multidimensional effects in forced convection subcooled boiling, in: Proceedings of the 9th International Heat Transfer Conference, 1990.

[10] L. Gilman, E. Baglietto, A self-consistent, physics-based boiling heat transfer modeling framework for use in computational fluid dynamics, Int. J. Multiph. Flow 95 (2017) 35–53, http://dx.doi.org/10.1016/j.ijmultiphaseflow.2017.04.018.

[11] R. Kommajosyula, Development and assessment of a physics-based model for subcooled flow boiling with application to CFD (Ph.D. thesis), 2020, pp. 25–50.

[12] P. Liu, X.B. Peng, Y.T. Song, X.D. Fang, S.H. Huang, X. Mao, Numerical simulation in a subcooled water flow boiling for one-sided high heat flux in reactor divertor, Fusion Eng. Des. 112 (2016) 587–593, http://dx.doi.org/10.1016/j.fusengdes.2016.05.010.

[13] S. Yu, J. Lu, C. Peng, Analyses of monoblocks divertor at one-sided high heat flux using rpi wall boiling model, Appl. Therm. Eng. 199 (2021) http://dx.doi.org/10.1016/j.applthermaleng.2021.117591.

[14] B. Končar, M. Tekavčič, A. Gajšek, M. Draksler, J. Fellinger, M. Richou, On the limitations of CFD modelling of flow boiling at high flow velocities and high heat fluxes, Int. J. Heat Mass Transfer 254 (2026) http://dx.doi.org/10.1016/j.ijheatmasstransfer.2025.127707.

[15] A. Gajšek, G. Kozmus, M. Tekavčič, M. Richou, B. Končar, Boiling flow visualization experiment scaled to divertor cooling conditions, Fusion Eng. Des. 218 (2025) http://dx.doi.org/10.1016/j.fusengdes.2025.115188.

[16] S.T. Yin, et al., A thermohydraulics correlation package for heat transfer design evaluations of NET plasma facing components, 1991, Final report, NET contract 90-81P.

[17] A.V. Dedov, A.T. Komov, A.N. Varava, V.V. Yagov, Hydrodynamics and heat transfer in swirl flow under conditions of one-side heating. Part 2: Boiling heat transfer. Critical heat fluxes, Int. J. Heat Mass Transfer 53 (2010) 4966–4975, http://dx.doi.org/10.1016/j.ijheatmasstransfer.2010.05.035.

[18] A.N. Varava, A.V. Dedov, E.M. Zakharov, S.A. Malakhovskii, A.T. Komov, V.V. Yagov, Study of pressure drop and heat transfer in a swirl flow with one-sided heating in a range of heat flowrates below boiling crisis, Therm. Eng. 56 (2009) 953–962, http://dx.doi.org/10.1134/S004060150911010X.

[19] J. Yan, Q. Bi, Z. Liu, G. Zhu, L. Cai, Subcooled flow boiling heat transfer of water in a circular tube under high heat fluxes and high mass fluxes, Fusion Eng. Des. 100 (2015) 406–418, http://dx.doi.org/10.1016/j.fusengdes.2015.07.007.

[20] G. Zhu, Q. Bi, J. Yan, H. Lv, Experimental study of subcooled flow boiling heat transfer of water in a circular channel under one-side heating conditions, Int. J. Heat Mass Transfer 119 (2018) 484–495, http://dx.doi.org/10.1016/j.ijheatmasstransfer.2017.11.111.

[21] J.H. Lim, M. Park, Studies on heat transfer coefficient of a circular tube with twisted tape insert for high heat flux cooling applications, IEEE Trans. Plasma Sci. 50 (2022) 459–469, http://dx.doi.org/10.1109/TPS.2022.3141820.

[22] ANSYS FLUENT theory manual, 2020, 2020th Edition.

[23] C.-Y. Han, P. Griffith, The mechanism of heat transfer in nucleate pool boiling, Int. J. Heat Mass Transfer 8 (1965) 887.

[24] J. Cieslinski, J. Polewski, J. Szymczyk, Flow field around growing and rising vapour bubble by PIV measurement, J. Vis. 8 (2005) 209.

[25] B. Mikic, W. Rohsenow, A new correlation of pool-boiling data including the effect of heating surface characteristics, ASME J. Heat Transf. 91 (1969) 245–250.

[26] V. Gnielinski, New equations for heat and mass transfer in turbulent pipe and channel flow, Int. Chem. Eng. 16 (2) (1976) 359–368.

[27] W.E. Kennel, Local Boiling of Water and Superheating of High Pressure Steam in Annuli (Ph.D. thesis), Massachusetts Institute of Technology. Department of Chemical Engineering, 1949.

[28] V. Divavin, V. Tanchuk, A. Shrubok, R. Watson, J. González, An experimental and numerical investigation of post-CHF heat transfer for one-sided heat load with highly sub-cooled flow boiling, Fusion Eng. Des. 31 (2) (1996) 189–200, http://dx.doi.org/10.1016/0920-3796(96)00436-X.

[29] V. Tolubinsky, D. Kostanchuk, Vapour bubbles growth rate and heat transfer intensity at subcooled water boiling, in: International Heat Transfer Conference, Begel House Inc., Danbury, 1970, pp. 1–11, http://dx.doi.org/10.1615/IHTC4.250.

[30] G. Kocamustafaogullari, M. Ishii, Interfacial area and nucleation site density in boiling systems, Int. J. Heat Mass Transfer 26 (1983) 1377–1387, http://dx.doi.org/10.1016/S0017-9310(83)80069-6.

[31] J.S. Murallidharan, B. Prasad, B. Patnaik, G. Hewitt, V. Badalassi, CFD investigation and assessment of wall heat flux partitioning model for the prediction of high pressure subcooled flow boiling, Int. J. Heat Mass Transfer 103 (2016) 211–230, http://dx.doi.org/10.1016/j.ijheatmasstransfer.2016.06.050.

[32] M. Nemitallah, M. Habib, R. Ben Mansour, M. El Nakla, Numerical predictions of flow boiling characteristics: Current status, model setup and CFD modeling for different non-uniform heating profiles, Appl. Therm. Eng. 75 (2015) 451–460, http://dx.doi.org/10.1016/j.applthermaleng.2014.09.036.

[33] X. Zhang, T. Yu, T. Cong, M. Peng, Effects of interaction models on upward subcooled boiling flow in annulus, Prog. Nucl. Energy 105 (2018) 61–75, http://dx.doi.org/10.1016/j.pnucene.2017.12.004.

[34] J. Gu, Q. Wang, Y. Wu, J. Lyu, S. Li, W. Yao, Modeling of subcooled boiling by extending the RPI wall boiling model to ultra-high pressure conditions, Appl. Therm. Eng. 124 (2017) 571–584, http://dx.doi.org/10.1016/j.applthermaleng.2017.06.017.

[35] S.R.G. Vadlamudi, A.K. Nayak, Impact of turbulence models on departure from nucleate boiling prediction based on CFD methodology, in: Critical Heat Flux and Multiphase Flow, Varanasi, India, 2018, b.

[36] P. Liu, P. Wang, Y. Guo, M. Tang, X. Peng, W. Wang, J. Ji, Q. Chen, X. Mao, Simulation of DNB-type critical heat flux (CHF) and pressure drop in subcooled flow boiling of water for tubes with twisted tape inserts under one-sided heating conditions, Fusion Eng. Des. 170 (2021) 112520, http://dx.doi.org/10.1016/j.fusengdes.2021.112520.

[37] M. Colombo, R. Thakrar, M. Fairweather, S.P. Walker, Assessment of semi-mechanistic bubble departure diameter modelling for the CFD simulation of boiling flows, Nucl. Eng. Des. 344 (2019) 15–27, http://dx.doi.org/10.1016/j.nucengdes.2019.01.014.

[38] M. Colombo, M. Fairweather, Accuracy of Eulerian–Eulerian, two-fluid CFD boiling models of subcooled boiling flows, Int. J. Heat Mass Transfer 103 (2016) 28–44, http://dx.doi.org/10.1016/j.ijheatmasstransfer.2016.06.098.

[39] Q. Li, M. Avramova, Y. Jiao, P. Chen, J. Yu, Z. Pu, J. Chen, CFD prediction of critical heat flux in vertical heated tubes with uniform and non-uniform heat flux, Nucl. Eng. Des. 326 (2018) 403–412, http://dx.doi.org/10.1016/j.nucengdes.2017.11.009.

[40] U.W. Mszanowski, THERMPROP 5.2 user's guide, 2006.

[41] R. Cole, A photographic study of pool boiling in the region of the critical heat flux, AIChE J. 6 (4) (1960) 533–538, http://dx.doi.org/10.1002/aic.690060405.

[42] N. Basu, G.R. Warrier, V.K. Dhir, Wall heat flux partitioning during subcooled flow boiling: Part 1 - model development, J. Heat Transf. 127 (2005) 131–140, http://dx.doi.org/10.1115/1.1842784.

[43] S.R.G. Vadlamudi, A.K. Nayak, CFD simulation of departure from nucleate boiling in vertical tubes under high pressure and high flow conditions, Nucl. Eng. Des. 352 (2019) 110150, http://dx.doi.org/10.1016/j.nucengdes.2019.110150.

[44] L. Tao, C. Hu, Y. Xie, Numerical simulation of subcooled boiling inside high-heat-flux component with swirl tube in neutral beam injection system, Plasma Sci. Technol. 16 (2014) 512–520, http://dx.doi.org/10.1088/1009-0630/16/5/12.

[45] M.S. Plesset, S.A. Zwick, The growth of vapor bubbles in superheated liquids, J. Appl. Phys. 25 (4) (1954) 493–500.

[46] M. Cooper, A. Lloyd, The microlayer in nucleate pool boiling, Int. J. Heat Mass Transfer 12 (8) (1969) 895–913.

[47] M. Lemmert, J. Chawla, Influence of flow velocity on surface boiling heat transfer coefficient, in: E. Hahne, U. Grigull (Eds.), Heat Transfer in Boiling, Academic Press and Hemisphere, New York, 1977, pp. 237–247.

[48] N. Basu, G.R. Warrier, V.K. Dhir, Onset of nucleate boiling and active nucleation site density during subcooled flow boiling, J. Heat Transf. 124 (4) (2002) 717–728, http://dx.doi.org/10.1115/1.1471522, Published Online: July 16, 2002.

[49] T. Hibiki, M. Ishii, Active nucleation site density in boiling systems, Int. J. Heat Mass Transfer 46 (2003) 2587–2601, http://dx.doi.org/10.1016/S0017-9310(03)00031-0.